

# Level-set modelling of the two-phase flow generated by a surface piercing body

Giuseppina Colicchio<sup>1,2</sup>, Maurizio Landrini<sup>1</sup> and John Chaplin<sup>2</sup>

1 INSEAN, The Italian Ship Model Basin, Roma, Italy. maulan@waves.insean.it  
2 Department of Civil & Environmental Engineering, Southampton University, UK

## 1 Introduction

The flow field around a ship is extremely complex, even for the simplest case of motion through calm water with constant forward speed. In particular, many vortical structures are originated by the ship motion. Some of them are directly related to ship breaking waves, *e.g.* [3]. In other cases, vorticity is created at the hull boundary and shed along and downstream the ship.

Here, we present our investigations on some fluid dynamic processes connected with the motion of a blunt structure piercing the air-water interface. We consider a two-dimensional prototype problem consisting in a vertical flat plate, moving forward with known velocity (*cf.* figure 1). This rather simple problem is meant to be roughly representative of the fluid phenomena occurring around the bow of a blunt ship and near a transom stern.

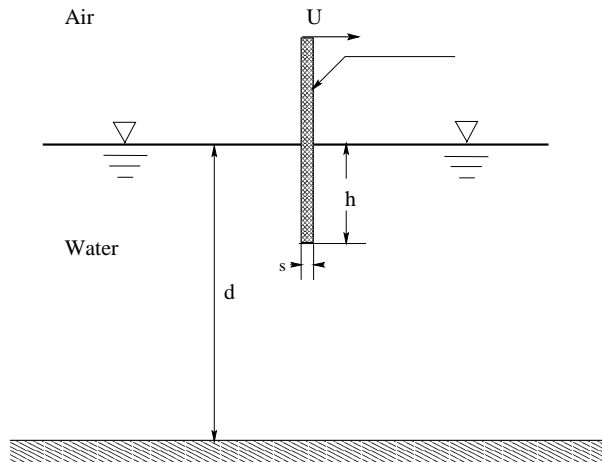


**Fig. 1:** Sketch of the considered problem and nomenclature adopted.

The problem is studied numerically by a Navier-Stokes solver with a Level-Set technique to capture the air-water interface.

The problem has been studied from an experimental point of view as well. Figure 2 shows a first comparison between numerical and experimental results. The experimental picture, in the background, is accompanied by the interface location (the blue line) and the vorticity contours obtained numerically. The flow is characterized by many complex features: vortex shedding from the immersed plate tip, wave breaking on the upstream side and (later on) breaking-induced air entrapment and wave breaking on the downstream side. Several plate velocities have been studied, with Froude number in the range 0.6-1.2. Different regimes of interaction between the vortical structures and the interface have been analysed, [6].

In the following, we focus on the computational method and details of the implementation are discussed through numerical results.

Experimental measurements of the interface deformation, of the pressure on the plate and of the velocity field are under development and will be presented at the Workshop to complement the physical interpretation of the flow.

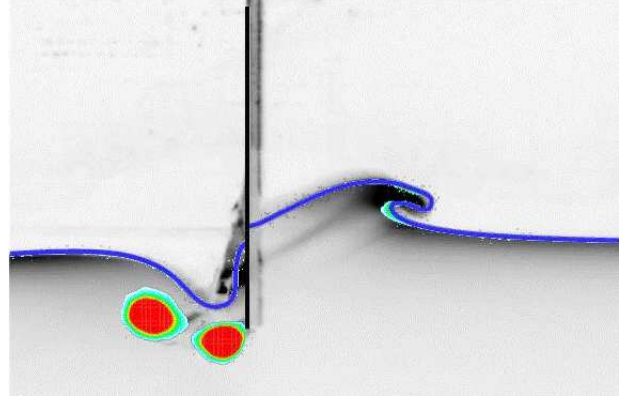


**Fig. 2:** Two-dimensional flow around a vertical plate moving from left to right,  $Fr = U/(gh)^{1/2} = 0.8$ ,  $Re = Uh/\nu = 10^7$ ,  $We = U^2 h\rho/\sigma = \infty$ . Interface and vorticity contours obtained from the numerical simulations are superimposed to the experimental flow visualization.

## 2 One-fluid model of two-phase flows

A possible approach to deal with interfacial flows is to consider the two phases as a continuous field where the generic fluid property, say  $f$ , is defined by patching the corresponding fields in the two phases, that is

$$f = \chi f_{air} + (1 - \chi) f_{water} . \quad (1)$$

A rapid but smooth transition from one phase to another is guaranteed by the bridge function  $\chi \in [0, 1]$ . In this framework, the evolution of the compound flow field is described by the Navier-Stokes equations for a single fluid and, in principle, there is no need to distinguish explicitly between the two phases. Continuity conditions of velocity and tangential stresses at the interface are automatically fulfilled, though in a "smoothed" sense, while surface-tension effects have to be modelled explicitly. Clearly, most of the numerical difficulties are shifted to the treatment of the bridge function. In the following, we will use a Level-Set approach to define the transition from one phase to another. Namely, the air-water interface is not explicitly followed but its position is captured as the zero level of a scalar field, defined in the whole computational domain. A laminar flow is assumed. The field equations are discretized by a finite-difference scheme, with second-order accuracy both in time and space. The spatial discretization is based on an upwind ENO scheme. The time discretization is based on a predictor-corrector method, with iterations, and on a variable-density projection method.

**2.1 Background fluid-flow solver** We assume that the evolution of the one-fluid system is governed by the Navier-Stokes equations

$$\begin{aligned} \nabla \cdot \mathbf{u} &= 0 \\ \rho \frac{D\mathbf{u}}{Dt} &= -\nabla p + 2\nabla \cdot \mu \mathbf{D} + 2\sigma\kappa\delta_S \mathbf{n} + \rho \mathbf{g} \end{aligned} \quad (2)$$

where the density  $\rho$  and the dynamic viscosity  $\mu$  vary across the interface. The term  $2\sigma\kappa\delta_S \mathbf{n}$  is the capillary force, with  $\sigma$  the surface tension,  $\mathbf{n}$  the normal to the interface,  $\kappa$  half the

interface curvature and  $\delta_S$  the Dirac function equal to unity on the interface and zero elsewhere. Finally,

$$(\mathbf{D})_{ij} = D_{ij} = \frac{1}{2} \left( \frac{\partial u_j}{\partial x_i} + \frac{\partial u_i}{\partial x_j} \right)$$

is the rate of strain tensor. Within the one-fluid formulation, the conditions at the interface between two viscous fluids, *e.g.* [7], are automatically captured. The explicit modelling of surface-tension effects is described later.

**TIME DISCRETIZATION** A second-order approximation in time of Eq. (2) can be written as:

$$\begin{aligned} \frac{\mathbf{u}^{n+1} - \mathbf{u}^n}{\Delta t} &= -\frac{\nabla p^{n+1/2}}{\rho^{n+1/2}} - [(\mathbf{u} \cdot \nabla) \mathbf{u}]^{n+1/2} \\ &+ \frac{[2\nabla \cdot \mu \mathbf{D}]^{n+1/2}}{\rho^{n+1/2}} + \frac{[2\sigma \kappa \delta_S \mathbf{n}]^{n+1/2}}{\rho^{n+1/2}} + \mathbf{g} \end{aligned} \quad (3)$$

and it is solved through a predictor-corrector scheme. Differently from most implementations, the corrector step is iterated until convergence is reached to improve stability and accuracy [2]. For brevity, we introduce the term

$$F(\mathbf{u}) = -(\mathbf{u} \cdot \nabla) \mathbf{u} + \frac{2\nabla \cdot \mu \mathbf{D}}{\rho} + \mathbf{g}$$

approximated by (different) Taylor expansions in both steps.

*Predictor step* The density and the surface tension at the time  $n + 1/2$  are approximated with those at time  $n - 1/2$ , and  $[F(\mathbf{u})]^{n+1/2}$  is obtained through a Taylor expansion from the previous time steps. The pressure gradient is written as:

$$\frac{\nabla p_0^{n+1/2}}{\rho^{n+1/2}} = \frac{\nabla p_0^{n+1/2}}{\rho^{n+1/2}} - \frac{\nabla p^{n-1/2}}{\rho^{n-1/2}} + \frac{\nabla p^{n-1/2}}{\rho^{n-1/2}},$$

and the two-step procedure to obtain the velocity  $\mathbf{u}_0^{n+1}$  reads:

$$\begin{aligned} \tilde{\mathbf{u}} &= \mathbf{u}^n + \Delta t \left\{ [F(\mathbf{u})]_0^{n+1/2} - \frac{\nabla p^{n-1/2}}{\rho^{n-1/2}} \right\} \\ \mathbf{u}_0^{n+1} &= \tilde{\mathbf{u}} + \Delta t \left\{ \frac{\nabla p^{n-1/2}}{\rho^{n-1/2}} - \frac{\nabla p_0^{n+1/2}}{\rho^{n+1/2}} + 2\sigma \frac{(\kappa \delta_S \mathbf{n})^{n-1/2}}{\rho^{n-1/2}} \right\} \end{aligned} \quad (4)$$

For an incompressible fluid, the second equation in (4) becomes:

$$\frac{\nabla \cdot \tilde{\mathbf{u}}}{\Delta t} = \nabla \cdot \left( \frac{\nabla(p^{n-1/2} - p_0^{n+1/2})}{\rho^{n-1/2}} + 2\sigma \frac{(\kappa \delta_S \mathbf{n})^{n-1/2}}{\rho^{n-1/2}} \right).$$

At time  $n + 1/2$ , the pressure is decomposed as  $p = p_{(st)} + p_{(nst)}$ . The first contribution results in the pressure jump at the interface due to the surface-tension effects,

$$\nabla^2 p_{(st),0}^{n+1/2} = \nabla \cdot \left( 2\sigma (\kappa \delta_S \mathbf{n})^{n-1/2} \right), \quad (5)$$

and it is completely independent of the density distribution. The second term  $p_{(nst)}$  is the pressure in the case without surface-tension effects:

$$\nabla \cdot \left( \frac{\nabla(p^{n-1/2} - p_{(nst),0}^{n+1/2})}{\rho^{n-1/2}} \right) = \frac{\nabla \cdot \tilde{\mathbf{u}}}{\Delta t}. \quad (6)$$

The solution of the Poisson equations (5) and (6) gives  $p_0^{n+1/2}$ ,  $\mathbf{u}_0^{n+1/2}$  follows from the second equation in (4), while the viscosity and density fields are defined once the interface has been captured by the Level-set technique discussed later. These data are used to start the iterative corrector step.

*Corrector step* At the  $k$ -th step of the corrector, the term  $[F(\mathbf{u})]_k^{n+1/2}$  is obtained by a centered Taylor expansion, and the pressure gradient is written as:

$$\frac{\nabla p_{(ns),k}^{n+1/2}}{\rho_{k-1}^{n+1/2}} = \frac{\nabla p_{(ns),k-1}^{n+1/2}}{\rho_{k-1}^{n+1/2}} + \frac{\nabla p_c}{\rho_{k-1}^{n+1/2}},$$

where  $p_c$  is a pressure-correction term arising from the approximate projection method:

$$\begin{aligned} \tilde{\mathbf{u}} &= \mathbf{u}^n + \Delta t \left\{ [F(\mathbf{u})]_{k-1}^{n+1/2} - \frac{\nabla p_{k-1}^{n+1/2}}{\rho_{k-1}^{n+1/2}} \right\} \\ \mathbf{u}_k^{n+1} &= \tilde{\mathbf{u}} + \Delta t \left\{ 2\sigma \frac{(\kappa \delta_S \mathbf{n})_{k-1}^{n+1/2}}{\rho_{k-1}^{n+1/2}} - \frac{\nabla p_c}{\rho_{k-1}^{n+1/2}} \right\} \end{aligned}$$

by solving the Poisson equations:

$$\begin{aligned} \nabla^2 p_{(st),k}^{n+1/2} &= \nabla \cdot \left( 2\sigma (\kappa \delta_S \mathbf{n})_{k-1}^{n+1/2} \right) \\ \nabla \cdot \left( \frac{\nabla p_c}{\rho_{k-1}^{n+1/2}} \right) &= \frac{\nabla \cdot \tilde{\mathbf{u}}}{\Delta t} \end{aligned}$$

As before, once the above Poisson equations have been solved, velocity, density and viscosity fields can be updated. Again, we note that density and viscosity depend on the iteration step  $k$  because of the motion of the interface. The iterative procedure is repeated until convergence is satisfied.

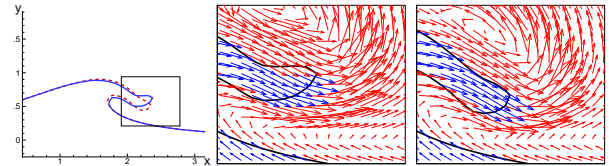
**SPATIAL DISCRETIZATION** For the spatial discretization, we have used staggered grid and  $x$ - and  $y$ -derivatives have been calculated using a second-order approximation and an Essentially Non-Oscillatory (ENO) scheme [1]. The application of second-order ENO schemes, requires the choice of a so-called "limiter function". One of the most commonly used limiters is the "minmod" which is known to be dissipative. This feature is usually accepted because it smooths the high normal gradient of the tangential velocity and further stabilizes the interface with a numerical viscosity. The so-called "superbee" is the most suitable limiter to capture the advection of a steep function. However its indiscriminate application whole over the domain is not suitable with more smoothed velocity profiles inside each one of the two phases. Though other limiters have been proposed, minmod and superbee have been selected because of their individual features and because of the possibility of a smooth patching from one to another allowing a more accurate advection of the velocity whole over the computational domain. In fact, we have introduced a variable coefficients limiter function  $m(a, b)$  in the form:

$$m(a, b) = \begin{cases} 0 & \text{if } ab < 0 \\ \max(\min(f|a|, |b|), \min(f|b|, |a|)) \text{sign}(a) & \text{if } ab \geq 0 \end{cases}$$

where the coefficient  $f$  is a function of the distance  $\phi$  from the interface:

$$f = \begin{cases} \frac{1}{2} \cos\left(\frac{\phi\pi}{\delta_{lim}}\right) + 1 & \text{if } |\phi| < \delta_{lim} \\ 1 & \text{if } |\phi| > \delta_{lim} \end{cases}$$

and  $\delta_{lim}$  is the interval of variation of the coefficients. The practical choice of  $\delta_{lim}$  will be discussed later.



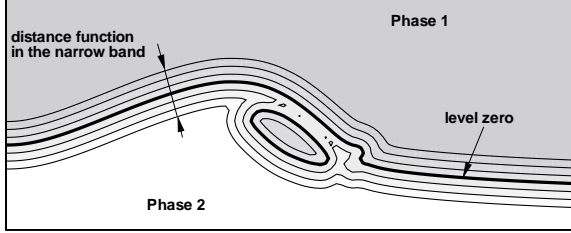
**Fig. 3: Comparison of the interface location with (dashed line) and without using (solid line) the variable-coefficient limiter function, for the test case considered in figure 2,  $t(g/h)^{1/2} = 4.0$ .**

Figure 3 shows the effect of using different limiter functions for the case shown in figure 2. In particular, the minmod limiter, solid line, produces a rather unphysical result with a "nose-up" plunging jet. This is due to a numerical diffusion of the air velocity field inside the water, *cf.* center plot, which is significantly reduced in the present formulation, dashed line and right plot.

We note that this formulation is valid for high Reynolds number. In fact, the tangential velocity would be physically smoothed by the higher fluid viscosity and the use of a superbee scheme would produce unphysical steepening of the tangential velocities at the interface.

In the final implementation, the algebraic systems arising from the discretization of the Poisson equations are solved by a GMRES technique, which we found rather efficient and easily portable on massive parallel computers.

**2.2 Interface capturing** The interface between the fluids is traced using a level-set function  $\phi$ , as introduced in [5]. A narrow band around the interface is characterized by its signed distance from the air-liquid interface, figure 4. The level-set function is used to define the bridge function  $\chi$ , adopted to smooth the flow variables across the interface. The explicit functional form of the bridge function depends on the considered variable, as discussed in the following.



**Fig. 4:** Definition of a distance function in a narrow band around the interface zero level when the forward plunging jet hits the underlying interface (*cf.* the test case considered in figure 2).

In particular, upon considering the density a function of  $\phi$ , we can write the continuity equation as:

$$\frac{\partial \rho}{\partial \phi} \left( \frac{\partial \phi}{\partial t} + \mathbf{u} \cdot \nabla \phi \right) = 0,$$

which gives the transport equation for the level-set function, as far as  $\partial \rho / \partial \phi \neq 0$ . The Lagrangian evolution of  $\phi$  does not preserve distances. Therefore, a periodic reinitialization of  $\phi$  is necessary to restore its geometrical meaning. The reinitialization, as introduced in [5], is based on:

$$\frac{\partial \phi}{\partial \tau} + \left( \frac{\nabla \phi \cdot \nabla \phi}{|\nabla \phi|} - 1 \right) \text{sign}(\phi) = 0, \quad (7)$$

where  $\phi$  evolves in the pseudo time  $\tau$  until stationary conditions are obtained. The standard solution procedure is based on an ENO scheme for the calculation of the spatial derivatives. As shown in [4], such schemes introduce an error at the interface. To alleviate the problem, [4], equation (7) can be solved by:

$$\phi_{i,j}^{l+1} = \begin{cases} \phi_{i,j}^n - \Delta \tau \left( \text{sign}(\phi_{i,j}^0) |\phi_{i,j}^l| - D_{i,j} \right) & \text{interface cell} \\ \phi_{i,j}^n - \Delta \tau \text{sign}(\phi_{i,j}^0) \left( \frac{\nabla \phi_{i,j}^l \cdot \nabla \phi_{i,j}^l}{|\nabla \phi_{i,j}^l|} - 1 \right) & \text{otherwise} \end{cases} \quad (8)$$

where

$$D_{i,j} = \frac{2\phi_{i,j}^0}{\sqrt{\frac{(\phi_{i+1,j}^0 - \phi_{i-1,j}^0)^2}{\Delta x^2} + \frac{(\phi_{i,j+1}^0 - \phi_{i,j-1}^0)^2}{\Delta y^2}}}$$

This procedure has been found to be more accurate when the interface is split into many branches, as the case presented in figure 5, without the need of introducing different level functions. In spite of this, we still observed the numerical smoothing of the interface for those cases with high curvature of the interface. For such cases, a more accurate solution can be obtained by adopting:

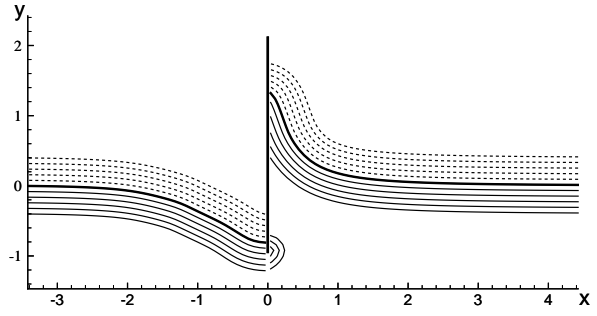


**Fig. 5:** Example of contour levels when the interface approaches the lower tip of the plate.

$$D_{i,j}^m = \frac{\phi_{i,j}^0}{\sqrt{A+B}}$$

$$A = \frac{\phi_{i+1,j}^0 \left( \frac{\phi_{i+1,j}^0 - \phi_{i,j}^0}{2} \right) + (\phi_{i,j}^0)^2 + \phi_{i-1,j}^0 \left( \frac{\phi_{i-1,j}^0 - \phi_{i,j}^0}{2} \right)}{\Delta x^2},$$

$$B = \frac{\phi_{i,j+1}^0 \left( \frac{\phi_{i,j+1}^0 - \phi_{i,j}^0}{2} \right) + (\phi_{i,j}^0)^2 + \phi_{i,j-1}^0 \left( \frac{\phi_{i,j-1}^0 - \phi_{i,j}^0}{2} \right)}{\Delta y^2}$$

which has the drawback that it does not smooth the oscillations at the interface and results in a poorer stability. Therefore, in the final implementation, at the interface we adopted a weighted combination of the two methods, that is

$$\phi_{i,j}^{l+1} = \phi_{i,j}^n - \Delta \tau \left( (\text{sign}(\phi_{i,j}^0) |\phi_{i,j}^l| - (a_{rs} D_{i,j} + a_m D_{i,j}^m)) \right). \quad (9)$$

In our experience,  $a_{rs} = 0.8$  and  $a_m = 0.2$  is a suitable choice. Figure 6 shows the time evolution of the percentage error in mass conservation. For all the simulations,  $d = 11h$  and the domain length is  $60h$ . A  $256 \times 144$  Cartesian grid is used. Near the plate, the grid is uniform and the cell dimensions are  $\Delta x = \Delta y = 0.046h$ . For distances from the plate larger than  $5h$  in the horizontal direction and larger than  $2h$  in the vertical direction, the grid is stretched in both directions by an exponential function. During the initial evolution, the three reinitializa-

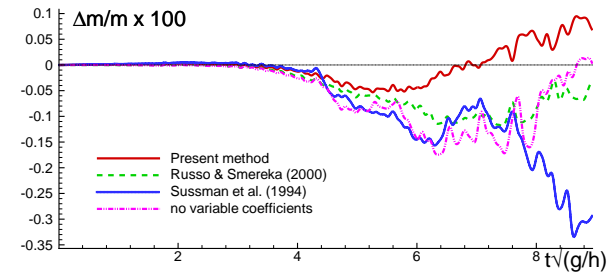


**Fig. 6:** History of mass conservation for the test case considered in figure 2

tion schemes behave in a similar manner and differences just to be visible with the formation of the forward plunging jet, as confirmed by the top plot of figure 7,  $t(g/h)^{1/2} = 4.0$ . At least up to the impact of the jet against the underlying interface,  $t(g/h)^{1/2} \sim 4.5$ , we observe a better conservation of the hybrid scheme (9). For longer evolutions, mass conservation by schemes (8) and (9) are roughly comparable but first comparisons with the experimental visualizations show the increasing inaccuracy for the former, with weaker and delayed splash up. The standard approach [5] is less and less reliable, as it is confirmed by the disappearance of the air cavity entrapped by the plunging jet and a smaller forward splash up.

**2.3 Smoothing across the interface** The coefficients of the limiter function are not the only quantities that are

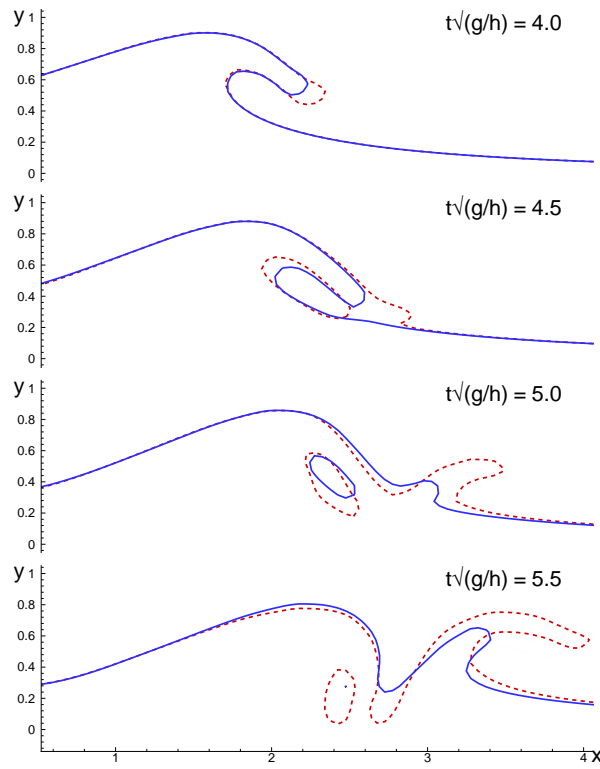


**Fig. 7:** Comparison of the interface location obtained by the standard level-set algorithm [5], solid line, by the improved level-set [4], dotted line, and by the present method, dashed line, for the test case of figure 2. From top to bottom, formation of the forward plunging jet, impact with the interface and formation of an entrapped air cavity.

smoothed across the interface. In particular, the solution of the Poisson equation for  $p_{(nst)}$  requires smoothing of the density across the interface to avoid (possibly divergent) numerical oscillations. Usually, the compound density is defined by a trigonometric bridge function. Therefore, the compound  $1/\rho$  function, entering in the equations, is steeper on the air-side, shifting in air most of the transition from the water to the air fields. In our experience, this reduces the stability of the method and reduces the accuracy of the solution. In the present implementation, we adopted the bridge function:

$$\rho(\phi) = \begin{cases} \rho_w & \text{if } (\phi - \delta_\rho c) < -\delta_\rho \\ \sqrt{\rho_w \rho_a} e^{\log(\frac{1}{2} \frac{\rho_w}{\rho_a}) \sin(\frac{\phi}{2\delta_\rho} (\phi - \delta_\rho c))} & \text{if } |\phi - \delta_\rho c| < \delta_\rho \\ \rho_a & \text{if } (\phi - \delta_\rho c) > \delta_\rho \end{cases} \quad (10)$$

where  $\rho_w$  and  $\rho_a$  are respectively water and air density and the constant coefficient  $c$  is chosen to conserve the total mass according to:

$$\int_{\delta_\rho(-1+c)}^{\delta_\rho(1+c)} \rho d\phi = \rho_w \delta_\rho (1-c) + \rho_a \delta_\rho (1+c).$$

In practice,  $c \simeq 0.5521$  for the air-water density ratio. Using (10) results in a more centered transition across the interface. The difference between using (10) and the usually adopted trigonometric bridge function becomes important in the resolution of local flow details, where the mesh can be relatively coarser and the solution is more sensitive to the smoothing region. This is exemplified in figure 8 where the solutions by the trigonometric bridge function, solid line, and by the smoothing function here proposed, solid line, are presented. The center plot shows the appearance of (growing) oscillations in the velocity field which eventually prevent the computation to proceed. These are absent in the present solution, right plot.

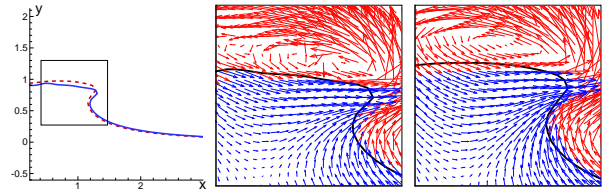


**Fig. 8:** Solution for the test case considered in figure 2 by using the trigonometric bridge function, solid line and center plot, and by using (10), dashed line and right plot.  $t(g/h)^{1/2} = 3.0$ .

It can be shown that, for a correct solution of the conservation equations, the inverse of the viscosity has to be smoothed across the interface, rather than the viscosity itself. Here, we have used:

$$\frac{1}{\mu}(\phi) = \begin{cases} \mu_w^{-1} & \text{if } \phi < -\delta_\mu \\ \frac{\mu_w^{-1} - \mu_a^{-1}}{2} \left( \frac{\sin(\frac{\pi\phi}{\delta_\mu})}{\pi} - \frac{\phi}{\delta_\mu} \right) + \frac{\mu_w^{-1} + \mu_a^{-1}}{2} & \text{if } |\phi| < \delta_\mu \\ \mu_a^{-1} & \text{if } \phi > \delta_\mu \end{cases}$$

We found that smoothing  $1/\mu$  rather than  $\mu$  becomes crucial when an accurate resolution of the air-flow dynamics is needed.

Finally, the Dirac function in the surface-tension is smoothed as:

$$\delta(\phi) = \begin{cases} 0 & \text{if } |\phi| \leq \delta_{st} \\ \frac{1}{2\delta_{st}} \left( \cos\left(\frac{\pi\phi}{\delta_{st}}\right) - 1 \right) & \text{if } |\phi| < \delta_{st} \end{cases}$$

In the present implementation, the amplitudes of the four smoothing intervals  $\delta_{lim}$ ,  $\delta_\rho$ ,  $\delta_\mu$  and  $\delta_{st}$  are fixed during the computations and satisfy:

$$\delta_{lim} \geq \delta_\rho = \delta_\mu > \delta_{st}.$$

The amplitude  $\delta_{lim}$  of the variable-coefficient limiter function should be larger than  $\delta_\rho$  to keep accurate the solution of the advection term in the transition region. Usually,  $\delta_{st} \geq 0.7\Delta x$  is sufficient to prevent oscillations in the solution of the corresponding Poisson equations. Such oscillations would induce unphysical parasite currents in both phases, though larger in air because of the density ratio. Therefore, if  $\delta_\rho > \delta_{st}$  the gradients of  $p_{(st)}$  decrease more rapidly, reducing the presence of unphysical currents in air side.

INSEAN research activity is supported by the Italian *Ministero per le Infrastrutture e Trasporti* through INSEAN Research Program 2003-05.

## References

- [1] A. Harten and S. Osher, Uniformly high-order accurate non oscillatory schemes, *SIAM J. Num. Anal.* **24** (1987) 279–309.
- [2] Y. Fraigneau J.L. Guermond and L. Quartapelle, Approximation of variable density incompressible flows by means of finite elements and finite volumes, *Comm. Num. Meth. Engng* **17** (2001) 893–902.
- [3] M. Landrini, A. Colagrossi, M. P. Tulin, Numerical Studies of Breaking Bow Waves Compared to Experimental Observations, In: Proc. 4<sup>th</sup> Numerical Towing Tank Symposium (2001), Hamburg (Germany).
- [4] Russo G. and Smereka P. (2000), A remark on computing distance functions. *J. Comp. Physics* **163**, pp. 51-67 (2000).
- [5] M. Sussman, P. Smereka and S. Osher, A Level Set Approach for Computing Solutions to Incompressible Two-Phase Flow. *J. Comp. Physics* **114** (1994) 146–159.
- [6] W.T. Tsai and D.K.P. Yue, Interaction between a free surface and a vortex wheel shed in the wake of a surface-piercing plate, *J. Fluid Mech.* **257** (1993) 691–721.
- [7] J.V. Wehausen and E.V. Laitone, *Handbuch der Physik*, ed. W. Fludge **9** (1960) 446-778.